

This discussion paper is/has been under review for the journal Atmospheric Chemistry and Physics (ACP). Please refer to the corresponding final paper in ACP if available.

Solar geoengineering using solid aerosol in the stratosphere

D. K. Weisenstein¹ and D. W. Keith^{1,2}

¹School of Engineering and Applied Science, Harvard University, Cambridge, MA, USA

²Kennedy School of Government, Harvard University, Cambridge, MA, USA

Received: 10 March 2015 – Accepted: 1 April 2015 – Published: 21 April 2015

Correspondence to: D. K. Weisenstein (dkweis@seas.harvard.edu)

Published by Copernicus Publications on behalf of the European Geosciences Union.

11799

Abstract

Solid aerosol particles have long been proposed as an alternative to sulfate aerosols for solar geoengineering. Any solid aerosol introduced into the stratosphere would be subject to coagulation with itself, producing fractal aggregates, and with the natural sulfate aerosol, producing liquid-coated solids. Solid aerosols that are coated with sulfate and/or have formed aggregates may have very different scattering properties and chemical behavior than do uncoated non-aggregated monomers. We use a two-dimensional chemical transport model to capture the dynamics of interacting solid and liquid aerosols in the stratosphere. As an example, we apply the model to the possible use of alumina and diamond particles for solar geoengineering. For 240 nm radius alumina particles, for example, an injection rate of 4 Mt yr^{-1} produces a global-average radiative forcing of 1.3 W m^{-2} and minimal self-coagulation of alumina yet almost all alumina outside the tropics is coated with sulfate. For the same radiative forcing, these solid aerosols can produce less ozone loss, less stratospheric heating, and less forward scattering than do sulfate aerosols. Our results suggest that appropriately sized alumina, diamond or similar high-index particles may have less severe technology-specific risks than do sulfate aerosols. These results, particularly the ozone response, are subject to large uncertainties due the limited data on the rate constants of reactions on the dry surfaces.

1 Introduction

Solar geoengineering, or Solar Radiation Management (SRM) is the possibility of deliberately introducing changes to the Earth's radiative balance to partially offset the radiative forcing of accumulating greenhouse gases and so lessen the risks of climate change. Most research on SRM has concentrated on the possibility of adding aerosols to the stratosphere, and essentially all atmospheric modeling of stratospheric aerosol injection has focused on increasing the loading of aqueous sulfuric acid aerosols

11800

(Rasch et al., 2008; Heckendorn et al., 2009; Niemeier et al., 2011; Pitari et al., 2014). The possibility that solid aerosol particles might offer advantages over sulfates, such as improved scattering properties, was first suggested almost two decades ago, but analysis has been almost exclusively limited to conceptual studies or simple radiative transfer models (Teller et al., 1997; Pope et al., 2012; Blackstock et al., 2009; Keith, 2010).

Any solid aerosol injected directly into the stratosphere for geoengineering purposes would be subject to coagulation with itself and with the natural background or volcanic sulfate aerosol. Aggregates of solid aerosols have very different physical structure and scattering properties than do liquid sulfate aerosol particles. The lifetimes and scattering properties of a solid aerosol are strongly dependent on these dynamical interactions, and the chemical properties of the aerosol depend on the extent to which it becomes coated by the ambient sulfate.

We have modified the Atmospheric and Environmental Research (AER) two-dimensional sulfate aerosol model (Weisenstein et al., 1997, 2007) to capture the dynamics of interacting solid and liquid aerosols in the stratosphere. Our model now includes a prognostic size distribution for three categories of aerosols: liquid aerosols, solid aerosols, and liquid-coated solid aerosols. The model's coalescence kernel has been modified and extended to parameterize the interactions of particles across size bins and between all combinations of the three categories. The surface area, sedimentation speed, and coalescence cross-section of an aggregate of solid particles depend on the geometry of the aggregate. The model parameterizes this physics using a fractal dimension and allows that fractal dimension to change with age or with a liquid coating.

Turning now to the context of this work, it is useful to divide overall consideration of the risks and efficacy of SRM into two components. First, the ability, or *efficacy*, of idealized SRM – conceived as a reduction in the solar constant – to compensate for the risks of accumulating greenhouse gases. And, second, the *technology-specific risks* of any specific engineered intervention that produces a change in radiative forcing. Uncertainty in the efficacy of SRM, the first component, rests on uncertainty in the

11801

climate's large-scale response to forcing. Results from a large set of climate models suggest that idealized SRM can do a surprisingly good job in reducing local and global climate change, which, in our view, is a primary motivation for continued research on SRM (Kravitz et al., 2014; Moreno-Cruz et al., 2011).

Evaluation of the technology-specific risks depends on the specific technology. For sulfate aerosols these risks include (a) ozone loss, (b) radiative heating of the lower stratosphere which causes changes in atmospheric temperature and dynamical transport, and (c) the fact that sulfates produce a relatively high ratio of downward scattering to upward scattering so that they substantially increase the ratio of diffuse to direct radiation (Kravitz et al., 2012) which in turn may alter atmospheric chemistry and ecosystem functioning (Wilton et al., 2011). In addition to the risks, it may be difficult to produce sufficiently large radiative forcings using SO_2 because of the decreasing efficiency at higher SO_2 inputs (Heckendorn et al., 2009).

The use of solid particles for SRM offers the *potential* to address all of the limitations of sulfate particles. Solid aerosols do not, for example, directly increase the stratospheric volume of the aqueous sulfuric acid that drives hydrolysis reactions, an important pathway through which sulfate aerosols cause ozone loss. In addition, some solid aerosols (e.g., diamond, alumina, or titania) have optical properties that may produce less heating in the lower stratosphere (Ferraro et al., 2011), and any solid with a high index of refraction can reduce forward scattering.

The use of solid aerosols, however, introduces new risks that require evaluation. The dry surfaces of the solid aerosols, for example, may catalyze reactions that cause ozone loss; and this risk is hard to evaluate because the rates of important chemical reactions remain unmeasured for substances such as diamond that are novel in the stratosphere. Moreover, by spreading the natural background sulfuric acid over a larger surface area as will occur when background sulfate coats the solid particles, the addition of solid aerosols will increase reactions that depend on sulfate surface area density rather than sulfate volume.

11802

Our motivation for studying solid particles is the possibility that they enable a decrease in the risks of SRM (e.g., ozone loss) or an increase in its efficacy such as the ability to produce larger radiative forcings, or an improved ability to “tune” the spectral or spatial characteristics of the radiative forcing (Blackstock et al., 2009; Keith, 2010).

5 This is in contrast to much of the prior literature that has focused on the potential of solid particles to deliver higher mass-specific scattering efficiency, thus reducing the amount of material needed to produce a given radiative forcing. We do not see this as an important motivation as it appears that the cost of lofting materials to the stratosphere is sufficiently low that cost is not an important barrier to implementation of SRM
10 (McClellan et al., 2012).

In this paper, our focus is on developing the tools and methodology for assessing the risks and performance of solid particles injected into the stratosphere for SRM. The tool described here is a new solid–liquid stratospheric aerosol model, and the methodology is a comparison of environmental side-effects such as ozone loss and forward scattering as a function of the global radiative forcing. We use aluminum oxide (alumina) aerosol as the primary example. Diamond appears to be superior to alumina in several respects, perhaps the most important being that it has minimal absorption in the thermal infrared. We examine diamond, but choose alumina as the primary example because there is a broad basis to examine alumina’s potential environmental impacts.
15 Unlike many other solid particles proposed for SRM, there is prior work examining alumina’s impacts on stratospheric chemistry (Danilin et al., 2001; Jackman et al., 1998; Ross and Shaeffer, 2014), work that was produced from NASA-funded studies starting in the late 1970’s motivated by concerns about the ozone impact of space shuttle launches (alumina is a major component of the shuttle’s solid rocket exhaust plume).
25 Moreover, alumina is a common industrial material with a high index of refraction for which there is substantial industrial experience with the production of nanoparticles (Hinklin et al., 2004; Tsuzuki and McCormick, 2004). With respect to potential environmental impacts of alumina deposition on Earth’s surface, the fact that aluminum oxides are a common component of natural mineral dust deposition provides a ba-

11803

sis for assessing impacts (Lawrence and Neff, 2009). For diamond, there is evidence that diamond nanoparticles are nontoxic to biological systems (Shrand et al., 2007). A much more substantive assessment of the human health and ecosystems impacts of any proposed solid aerosol would be required, however, prior to serious consideration
5 of their use for geoengineering.

The remainder of this paper is organized as follows. The solid–liquid model is presented in Sect. 2, results for geoengineering injection of alumina and diamond in Sect. 3, and discussion in Sect. 4.

2 Aerosol model

10 We have incorporated solid aerosols into the AER 2-D sulfate aerosol model (Weisenstein et al., 1997, 2007), which employs a sectional aerosol scheme. The modified model has three separate classes of aerosols, each with its own size distribution: solid particles, liquid $\text{H}_2\text{SO}_4\text{--H}_2\text{O}$ particles, and mixed solid–liquid particles. To fully specify the mixed particles we keep track of the volume of liquid $\text{H}_2\text{SO}_4\text{--H}_2\text{O}$ solution coating the mixed particles. Unlike liquid particles that coagulate into larger spheres, solid
15 particles coagulate into fractal structures with more complex properties. The fractal properties are required to predict the effective size of the particles appropriate to determining coagulation interactions and gravitational settling. Fractal properties are also needed to determine the condensation rate of H_2SO_4 gas onto alumina particles and the aerosol surface area density which is important to heterogeneous chemistry and ozone depletion.
20

The base AER 2-D model includes the sulfur-bearing source gases DMS, CS_2 , H_2S , OCS, and SO_2 emitted by industrial and biogenic processes (Weisenstein et al., 1997, 2007). MSA, SO_2 , SO_3 , and H_2SO_4 are chemical products. Chemical reactions affecting sulfur species are listed in Weisenstein et al. (1997) and their rates have been
25 updated according to Sander et al. (2011). Values of OH and other oxidants are taken from previous calculations of the AER 2-D model with full ozone chemistry (Weisen-

11804

stein et al., 2004) for model runs not requiring full chemistry. The model's 2-D transport is prescribed based on calculations by Fleming et al. (1999), which employed observed temperature, ozone, water vapor, zonal wind, planetary waves, and QBO, and represents a climatological average over the years 1978–2004. The domain is global, from the surface to 60 km, with resolution of 1.2 km in the vertical and 9.5° in latitude. Though the model is primarily suited to modeling the stratosphere and upper troposphere, it does contain a parameterization of tropospheric convection (Dvortsov et al., 1998) that serves to elevate SO₂ concentrations in the tropical upper troposphere.

The AER 2-D aerosol model was evaluated in SPARC (2006), for both nonvolcanic conditions and in the period following the eruption of Mt Pinatubo, and was found to be among the best 2-D and 3-D models available at that time.

Sulfate aerosols are produced by binary homogeneous nucleation of H₂SO₄ and H₂O, primarily in the tropical tropopause region, and their size is modified by condensation and evaporation of gas-phase H₂SO₄ and by coagulation among particles (Brock et al., 1995; Hamill et al., 1997). Sulfate aerosol particles are assumed to be liquid spheres with equilibrium composition (H₂SO₄ and H₂O fractions) determined by the local grid box temperature and water vapor concentration (Tabazadeh et al., 1997). The model uses a sectional representation of particle sizes, with 40 sulfate aerosol bins representing sizes from 0.39 nm to 3.2 μm by volume doubling. Particle distributions are also modified by sedimentation and by rainout/washout processes in the troposphere.

Solid particles are modeled with a similar sectional representation; in this case it is the number of monomers per particle that is doubled in successive bins. Only the monomers, the primary particles directly emitted into the atmosphere, are spherical. Larger particles produced by coagulation assume fractal structures that are defined by a fractal dimension D_f that determines how the size of an aggregate of particles is related to the number of primary particles. The radius of gyration R_g of a fractal (the root-mean-square distance from the center of mass) is given by:

$$R_g = R_0(N_i/k_f)^{(1/D_f)}$$

11805

where R_0 is the primary particle radius, N_i the number of monomers in the fractal of bin i , and k_f is a prefactor (Filippov et al., 2000; Maricq, 2007). Thus particle mass is proportional to $R_g^{D_f}$.

Surface area density (SAD) for fractal particles can be parameterized with an effective radius R_{eff} which can be related to primary radius and the number of monomer cores in the particle:

$$R_{\text{eff}} = R_0(N_i/k_h)^{(1/D_h)}$$

$$\text{SAD}_i = (4\pi R_0^2) \cdot (N_i/k_h)^{(2/D_h)}$$

where D_h and k_h are the scaling exponent and prefactor specific to surface transfer processes. With fractal dimension $D_f < 2.0$, D_h can be assumed equal to 2.0. With $D_f > 2.0$, D_h can be assumed equal to D_f (Filippov et al., 2000). When $D_h = 2.0$, the surface area of a fractal particle is equal to the surface area of the monomer multiplied by the number of monomers in the aggregate. This formalism is most appropriate for large values of N_i (i.e., greater than 100). For consistency at small values of N_i , we assume that $k_f = k_h = 1$, since we find that simulations producing only small N_i values are most efficient for geoengineering.

The solid particles are allowed to interact with background stratospheric sulfate particles by coagulation, and with gas phase H₂SO₄ and H₂O by condensation and evaporation. We use R_g as the particle radius when calculating the coagulation kernel, the probability that two particles will combine into one on collision (Maricq, 2007). The condensation rate depends on particle surface area, and secondarily, on a radius of curvature for the Kelvin correction. We use R_0 as the radius-of-curvature in the condensation equation, since gas molecules see the individual monomers making up the fractal. Above about 35 km, coated particles will lose their sulfate coating by evaporation and become dry again. We model mixed-phase particles by tracking particle number per bin and mass of H₂SO₄ per bin in the mixed particles. Volume and surface area of the mixed particles depends also on the H₂O present in the equilibrium H₂SO₄-H₂O solution.

11806

The sedimentation velocity of fractal particles represents a balance between the gravitational force, proportional to particle mass, M_p , and the drag force, proportional to the two-dimensional surface area projection of the particle, A_{2-D} , and modified by the Cunningham slip-flow correction, G , which accounts for larger sedimentation velocities with lower air density (Seinfeld and Pandis, 2006). We obtain sedimentation velocity W_{sed} from

$$W_{\text{sed}} = (M_p g R_g G) / (6 \eta A_{2-D}),$$

where η is the viscosity of air and g the gravitational constant. For spheres, W_{sed} is proportional to R^2 , whereas for uncoated fractal particles with $D_f \geq 2$, the area is taken to be πR_g^2 and W_{sed} is proportional to $G \cdot N^{(D_f-1)/D_f}$. When $D_f < 2$, the fractal is porous and the area is $N \cdot \pi R_0^2$, yielding a W_{sed} proportional to $G \cdot N^{(1/D_f)}$ (Johnson et al., 1996). We take the Reynolds number (a factor in the drag coefficient) and the Knudsen number (the primary term in the Cunningham slip-flow correction) to be proportional to R_g in all fractal cases. For coated particles, the particle mass, M_p , is the sum of the solid particle mass and $\text{H}_2\text{SO}_4\text{-H}_2\text{O}$ mass, and particle radius is taken to be R_g increased by the thickness of a uniform coating. However, when the radius of a sphere enclosing the total particle volume is larger than R_g plus a monolayer of H_2SO_4 , we use the spherical radius rather than R_g .

3 Model results

Before turning to the results, we use the following sub-section to describe (and provide some rationale for) the solid aerosol particles that we choose as test cases, and then in Sect. 3.2 we describe a few results regarding the sedimentation of aggregates that are useful in understanding the model results.

11807

3.1 Test cases: alumina and diamond aerosol particles

Several prior studies have examined a range of possible solid aerosols and performed some simple optimizations (Teller et al., 1997; Pope et al., 2012; Blackstock et al., 2009). For simplicity we only considered spherical dielectric particles made of materials that have negligible solubility in the aqueous sulfuric acid found under typical stratospheric conditions. An ideal material for SRM would have (a) a high index of refraction, (b) a relatively low density, (c) negligible absorption for both solar and thermal infrared spectral regions, and finally (d) it should have well understood surface chemistry under stratospheric conditions. In addition, even though this research is exploratory, materials are more plausible as candidates for deployment for SRM if they have low and well understood environmental toxicity and if there is a track record of production of industrial quantities of the material in the appropriate half micron size regime.

We chose alumina, or aluminum oxide (Al_2O_3), as our primary test case because it has a relatively high index of refraction ($n = 1.77$ in the middle of the solar band) and because there is a substantial literature on its chemistry (Molina et al., 1997; Sander et al., 2011) and stratospheric chemical impact (Danilin et al., 2001; Jackman et al., 1998). However, alumina has infrared absorption bands in the thermal infrared that will reduce its net radiative forcing and will cause some heating of the lower stratosphere (Ross and Schaeffer, 2014).

We chose diamond as a secondary test case because of its near-ideal optical properties: it has a very high index ($n = 2.4$) and negligible absorption for both solar and thermal infrared spectral regions. Despite this we did not choose diamond as the primary test case because there is minimal data about the chemistry of relevant compounds on diamond surfaces under stratospheric conditions, and because the ability to produce sub-micron material at industrial scale is much less certain than it is for alumina.

Alumina is an important industrial material as a precursor for aluminum production and for a variety of uses from sunscreen compounds applied to the skin to indus-

11808

trial catalysis. The global production rate is approximately 100 Mtyr^{-1} (USGS, 2014). There is a very large body of experience in making alumina nanoparticles. For example, liquid-feed flame spray pyrolysis is used to make structured nanoparticles of alumina in quantities greater than 1 ktyr^{-1} (Hinklin et al., 2004).

5 As we will see, the optimal size for a spherical alumina particles used as a scatterer in the stratosphere is of order 200 nm radius. Most of the industrial effort is focused on making smaller particles for catalysis but there are examples of production of relatively monodisperse particles with radii greater than 50 nm (Hinklin et al., 2004; Tsuzuki and McCormick, 2004).

10 For the purposes of this paper we will assume that it is possible to make roughly spherical alumina particles with a size range between 50 and 400 nm radius. This is a working assumption that seems plausible based on the very large technical literature (> 1000 papers in the last decade on alumina nanoparticles) and industrial base devoted to production of these materials. But it is simply an assumption. A significant effort involving experts from industry and academia would be required to meaningfully
15 asses the difficulty of producing large quantities of alumina with a suitable size and morphology for solar geoengineering.

There is rapidly growing industrial production of sub-micron diamond powders (Krueger, 2008), so there is no doubt that particles with appropriate morphology can
20 be produced. However, the industrial production volumes and academic literature on production technologies are far smaller than for alumina.

3.2 Factors controlling settling of aggregates

As discussed above, the dynamics of aggregated particles depend on their fractal dimension D_f . No observational data on the fractal dimension of $\sim 100 \text{ nm}$ hard spheres
25 aggregating under stratospheric conditions is available. As a guide, we adopt the value of D_f obtained in studies of the formation of fractal alumina aggregates from much smaller monomers at atmospheric pressure produced by combustion and oxidation of

11809

liquid aluminum drops that can result from burning solid rocket fuel. These studies, which produced aggregates of approximately $1 \mu\text{m}$ composed of primary particles of a few tens of nanometers in diameter, determined that the fractal dimension D_f for alumina is 1.60 ± 0.04 (Karasev et al., 2001, 2004), implying a sparsely-packed fractal.

5 The fractal dimension for a given material has been found to be invariant for a wide range of R_0 and N_i values. For comparison, soot aggregates typically have D_f values of ~ 2.0 (Kajino and Kondo, 2011; Maricq and Nu, 2004), while a value of 3.0 is appropriate for liquid particles which remain spherical upon coagulation. The density of alumina particles is taken to be 3.8 g cm^{-3} and that of diamond to be 3.5 g cm^{-3} . We
10 assume the same fractal dimensions for diamond as for alumina.

Sedimentation velocity strongly influences stratospheric lifetimes. Figure 1a shows sedimentation velocities as a function of altitude for uncoated alumina particles for monomer radii from 80 to 320 nm. Shown are sedimentation velocities for individual monomers and for fractals with $N = 4$ and $N = 32$, all with fractal dimension $D_f = 1.6$.
15 $N = 32$ fractals are not shown for monomers larger than 160 nm because no such large fractals form in our simulations, however we do show $N = 256$ fractals with 80 nm monomers. Alumina monomers fall at a faster rate than sulfate particles of the same diameter, given their greater density (3.8 g cm^{-3} for Al_2O_3 , approximately 1.7 g cm^{-3} for stratospheric $\text{H}_2\text{SO}_4\text{-H}_2\text{O}$ particles), and diamond particles (not shown) fall only slightly
20 slower than alumina particles of the same size owing to 8 % smaller density. Fractal particles fall faster than the monomers they are composed of in the troposphere and lower stratosphere, but at the same rate in the middle and upper stratosphere where the Knudsen number $Kn > 1$ and the slip-flow correction has the opposite size dependence as the other terms. Figure 1 also shows the model's average upward advective
25 velocity in the tropics as a function of altitude for comparison. Where sedimentation velocity exceeds average upwelling velocity, we expect alumina lifetime and vertical extent to be greatly impacted. This occurs only above 30 km for 80 nm monomers, but above 24 km for 160 nm monomers and 19 km for 240 nm monomers. For 240 and 320 nm monomers injected into the tropics at 20–25 km altitude, only a fraction of the

11810

injected mass will be lofted to higher altitudes and distributed to high latitudes by the Brewer–Dobson circulation.

It is known that soot particles, which form fractals similar to alumina particles, eventually assume a more compact structure in the atmosphere after acquiring a liquid coating (Kajino and Kondo, 2011; Mikhailov et al., 2006). Observations on the liquid uptake properties of alumina and their potential shape compaction are not available. For simplicity, we assume that the alumina particles are hydrophobic until they are coated with a sulfate-water mixture by coagulation with existing sulfate particles, and then they may take up additional H_2SO_4 and H_2O by condensation. The effects of this assumption are expected to be small under non-volcanic conditions, as most (> 95%) stratospheric sulfate exists in condensed form. To test the potential effect of compaction of liquid-coated solid alumina particles, we perform additional model calculations assuming that the wetted particles change their fractal dimension D_f from 1.6 to 2.8, and their SAD scaling exponent D_h from 2.0 to 2.8, likely the maximum compaction that could be achieved. While a time lag from initial wetting to shape compaction may be appropriate, we assume instantaneous compaction on wetting for calculations labeled “compact coated” as a way to bracket the effect. When the compacted particles lose their H_2SO_4 by evaporation, they are assumed to retain their compact shape. Sedimentation velocities for these coated and compacted particles are shown in Fig. 1b. In this case, higher order fractals fall at faster velocities than their respective monomers at all altitudes, which will affect the lifetime of alumina and its calculated atmospheric burden.

3.3 Aerosol distribution and burden

We model geoengineering by injection of alumina particles for a number of parametric model scenarios to evaluate the effect of (1) injected particles size, (2) injection rate, and (3) the fractal geometry of sulfate-coated alumina particles. For all scenarios, injection occurs in a broad band from 30° S to 30° N and from 20–25 km in altitude. This is the same injection region used in Pierce et al. (2010) and was chosen to maximize

11811

the global distribution and residence time of geoengineered aerosols while minimizing localized injection overlaps. We assume that it is feasible to emit alumina particle monomers with a uniform diameter, either by a flame process at the injection nozzle or by releasing prefabricated particles. Particles are released continuously at injection rates of 1, 2, 4, or 8 Mtyr^{-1} , all as monomers of a single radius (80, 160, 240, or 320 nm). Emissions are continuous in time and the simulations are continued for approximately 10 years until a steady atmospheric concentration is reached. Alumina particles that become coated with sulfate are treated either as retaining their sparse structure with fractal dimension D_f of 1.6 or instantaneously becoming more compact fractal particles with D_f of 2.8. We use a 2-D model for computation efficiency in this first evaluation of geoengineering by solid particle injection, and thus we implicitly mix the injected material into zonally-uniform bands dictated by the model’s spatial resolution of 9.5° latitude by 1.2 km altitude. The impact of this simplification, along with the neglect of enhanced coagulation in injection plumes, will be discussed in Sect. 4.

We first examine the calculated concentration and size distribution of atmospheric alumina under a geoengineering scenario with an injection rate of 1 Mtyr^{-1} , assuming no particle compaction on coating with sulfate. Figure 2, top panels, shows the atmospheric concentration of alumina (ppbm) with injection of 80 nm monomers and 240 nm monomers. Significant alumina concentration exist up to 40 km when 80 nm particles are injected, but only below 30 km for injection of 240 nm particles due to the difference in sedimentation speeds. Total stratospheric burden of alumina with 80 nm monomers injected is almost double that with 240 nm monomers injected. The lower panels of Fig. 2 show the concentration of particles (cm^{-3}) for the same cases. Particle concentrations of up to 25 cm^{-3} are found for 1 Mtyr^{-1} injection of 80 nm monomers but remain less than 3 cm^{-3} for injection of 240 nm monomers. The particle concentration drops away from the injection region as the monomers coagulate into fractals and have time to settle downward. The low number densities with $R_0 = 240$ nm result in minimal coagulation between alumina particles.

The distribution of stratospheric alumina mass into monomers and fractals is shown in Fig. 3 at the equator with 80 nm monomers injected (panel a) and for the global average with 80, 160, and 240 nm monomers injected, all with 1 Mtyr^{-1} of emissions. With injection of 80 nm monomers, 27 % of the mass remains in monomers at the equator, with no more than 13 % of the mass in any size bin with 2 or more monomers in the fractal. Some fractal particles comprised of 1024 monomers exist. At higher latitudes, the monomer fraction drops and the proportion in higher order fractals increases, as seen in the global average (panel b). The fraction of monomers coated, shown as the blue portion of each bar, increases with distance from the tropical injection region. Coated fractions also increase with increasing numbers of monomers per fractal particle. This reflects both the longer residence time of the larger particles and their large cross-section, which enhances coagulation with sulfate particles. Virtually all of the alumina mass is coated for fractals with more than 128 monomers per particle. Alumina in the troposphere is almost all coated with sulfate due to the large sulfate concentrations there, though alumina concentrations are small. With injection of 160 nm monomers, 71 % of the global mass remains in monomers, and fractals composed of only 2–16 monomers are found. With injection of 240 nm monomers, 94 % of the mass remains in monomers, and with 320 nm monomers injected, 98 % is monomers. Larger fractions of the alumina mass are coated in these latter cases.

The mass fraction in monomers vs. higher order fractals varies with injection rate. Figure 4a shows mass fraction vs. the number of monomers per particle for injection of 80 nm monomers at rates varying from 1 to 8 Mtyr^{-1} . As the injection rate increases, the mass fraction of monomers decreases while the peak distribution shifts to larger fractals. At injection rates of 2, 4, and 8 Mtyr^{-1} , the size distribution peaks at 32, 64, and then 128 monomers per particle, and fractals composed of 2000 monomers are found. Figure 4b shows a similar figure with injection of alumina as 160 nm radius monomers. Because these particles contain 8 times the mass of the 80 nm monomers, particle concentrations are considerably smaller and coagulation less effective. Fractals never contain more than 128 monomers even with 8 Mtyr^{-1} of emission. For injection

11813

of 240 nm monomers (Fig. 4c), 70 % of the particles remain as monomers even with 8 Mtyr^{-1} of emission, and no fractals exceed 16 monomers. For injection of 320 nm monomers (not shown), no fractals exceed 4 particles even with 8 Mtyr^{-1} of emission.

Figure 5a shows the stratospheric alumina burden as a function of injection rate for four different monomer radii. Alumina burden is seen to be approximately linear with emission rate. This is in contrast to a more strongly decreasing rate of change with increasing emissions seen for geoengineering by injection of SO_2 (Heckendorn et al., 2009) or H_2SO_4 (Pierce et al., 2010). In the case of sulfur injection, particles that grow to larger spherical sizes have shorter atmospheric residence times. For alumina particles with sparse fractal structure ($D_f = 1.6$), the larger particles do not increase their sedimentation velocities in the middle and upper stratosphere, resulting in residence times remaining almost constant over the alumina size distribution. The cases that produce the fewest fractals ($R_0 = 240$ and 320 nm) have the most linear response. The calculated atmospheric burden for diamond (not shown) is almost identical to that for alumina of the same size injected monomer. Also shown in Fig. 5 as dashed lines are simulations with coated alumina particles assumed to adopt a more compact fractal shape ($D_f = 2.8$). For these scenarios, total stratospheric burden is reduced due to the faster sedimentation of the coated particles, while the mass fraction in monomers is increased due to fewer high-order fractals to scavenge the monomers. Only the 80 and 160 nm cases show significant differences under the assumption that coated particles become more compact.

The stratospheric burden of sulfate is shown in Fig. 5b under various geoengineering scenarios. Thick lines (left hand axis labels) represent the total stratospheric burden of condensed sulfate as a function of geoengineering injection rate while thin lines (right hand axis labels) represent the fraction of stratospheric liquid sulfate on the surface of alumina particles. With injection of 80 nm alumina monomers, total stratospheric sulfate increases above background for injections less than 1.5 Mtyr^{-1} , but then decreases with higher injection rates. Up to 86 % of the total stratospheric sulfate is found on alumina particles in these cases, a result of the large alumina surface area available and

11814

high coagulation rates with large fractals. Alumina injection cases with larger monomer diameters lead to decreases in the total stratospheric burden of liquid sulfate because of the faster sedimentation of the larger alumina particles along with their sulfate coatings. The maximum decrease in total stratospheric sulfate is about 30 %. The fraction of total stratospheric sulfate found on alumina particles is as much as 82 % with 160 nm monomers, 61 % with 240 nm monomers, and 32 % with 320 nm monomers. The calculated thickness of the sulfate coating on alumina particles in the stratosphere varies from 5 to 15 nm with 80 nm monomers and from 10 to 40 nm with 240 nm monomers with 1 Mtyr⁻¹ of injection. However, as the geoengineering emission rate increases, the sulfate layer on alumina particles becomes thinner since the stratospheric sulfate burden will then be distributed over a larger alumina surface area.

3.4 Radiative forcing assessment

Alumina particles are known to be more efficient scatterers than sulfate particles, and thus are expected to be more efficient per unit mass for geoengineering applications. Figure 6 compares the Mie scattering properties of alumina and diamond monomers and sulfate particles as a function of particle radius. Figure 6a shows upscatter cross sections for the three particle types. The sulfate profile is fairly flat, with a cross section of about 0.3 for particles greater than 0.5 μm , whereas the alumina profile shows a 30 % drop from its peak of 0.6 between 0.2 and 0.6 μm to 0.4 at 2 μm . The diamond profile shows a peak of 0.9 between 0.15 and 0.5 μm , dropping to about 0.55 at radii greater than 1.2 μm . Figure 6b shows strong peaks in upscatter per unit volume for alumina and diamond monomers as a function of radius. In contrast, sulfate particles exhibit a much flatter function of upscatter per unit volume as a function of radius. Alumina monomers scatter most efficiently per unit particle volume at about 200–250 nm. At this radius, they have three times the upscatter per unit volume as sulfate particles. Upscatter per unit mass however, due to the difference in density of alumina relative to sulfate, shows less contrast. For diamond monomers, the upscatter per unit volume peaks at around 150 nm radius, with over twice the peak upscatter of alumina monomers.

11815

Figure 6c shows the ratio of downscatter to upscatter for alumina, diamond, and sulfate as a function of radius. Alumina monomers have about half the downscatter per unit of upscatter as sulfate particles, while diamond monomers have half the downscatter of alumina. Thus in geoengineering applications, alumina and diamond would scatter radiation back to space without a simultaneous significant increase in diffuse radiation at the surface.

We use a Mie scattering code which integrates the scattering function over spectral bands and scattering angles as a function of particle size (monomers and fractals) using an efficient impulse-function method. Multiple scattering is ignored as solid particle optical depths are small. We follow Rannou et al. (1999) for scattering by fractals. Figure 7a shows the radiative forcing functions ($\text{W m}^{-2} \text{Mt}^{-1}$) obtained by our scattering code as a function of monomer radius and fractal size (number of cores per particle). Scattering by 80 nm alumina monomers is much less efficient (factor of 4) than scattering by 160 nm alumina monomers. There is little difference in scattering between 240 and 320 nm alumina monomers, both with about 50 % greater RF per megaton than 160 nm monomers. Fractals scatter much less efficiently than monomers. A fractal aggregate of two cores scatters only 50 % as much radiation per megaton as a corresponding monomer, and higher order fractals scatter even less efficiently. An aggregate of 16 alumina monomers has negligible scattering. The functions with fractal dimension of both $D_f = 1.6$ (solid lines) and $D_f = 2.8$ (dashed lines, labeled “compact coated”) are shown for alumina, however, this produces only a minor difference in radiative forcing per megaton. The radiative forcing function for diamond with 160 nm monomers (the radius of peak backscatter efficiency) shows significantly greater forcing than alumina, 2.7 times greater than 160 nm alumina monomers and 1.8 times greater than 240 nm alumina monomers.

We obtain averages of solid aerosol mass in each bin size (monomers and fractals) integrated vertically and averaged over latitude and season. For purposes of radiative forcing, we assume that solid particles with thin sulfate coatings behave the same as bare particles. The integrated and averaged aerosol mass per bin is multiplied by the

spectrally-integrated radiative forcing per megaton for each bin to obtain the total radiative forcing for each geoengineering scenario. The radiative forcing due to alumina is shown in Fig. 7b as a function of injection rate for the cases with 80, 160, 240, and 320 nm monomer injections. Cases with 80 nm monomer injections have very low RF, due both to inefficient scattering for monomers of that size, and the large proportion of fractals to monomers. The RF for the 80 nm injection case increases very little with increasing emissions, as increasing emissions produces fractals composed of more than 64 monomers which produce almost no scattering per megaton. The case with injection of 320 nm monomers produces less RF than the case with injection of 240 nm monomers. Though monomers of 320 nm produce slightly more RF per megaton than monomers of 240 nm, the 320 nm injection cases yield a smaller burden due to their faster sedimentation rates. Injection of 240 nm monomers is found to produce the most radiative forcing per megaton of alumina emissions, consistent with the peak of the upscatter per unit volume curve shown in Fig. 6a. We calculate radiative forcing for diamond injections of 160 nm monomers. Atmospheric burden of diamond is very similar to that for alumina of the same radius, but RF is much larger owing to more efficient scattering. Diamond injection at a rate of 4 Mtyr^{-1} results in -2.0 W m^{-2} of forcing, while the same alumina injection results in only -1.3 W m^{-2} of forcing. The increase in downward diffusive flux is also calculated by our radiative forcing code and is shown in Table 1 for selected cases which each produce -2 W m^{-2} of forcing.

Our method produces only a globally-averaged value of radiative forcing by solid particles. Our results are not meant to be of high accuracy, as they are limited by the index of refraction data, uncertainties in fractal scattering, and our averaging method. Nevertheless, it is useful to obtain ballpark estimates of radiative forcing for comparison with sulfate geoengineering, and relative efficiencies among solid particle scenarios as a function of emitted monomer diameter. The RF plot in Fig. 7b shows radiative forcing from two sulfur geoengineering scenarios. The scenario results were calculated with the AER 2-D model, as applied in Heckendorn et al. (2009) and Pierce et al. (2010) but using the radiative scattering code applied to alumina and diamond.

11817

Note that we plot them here relative to the total SO_2 or H_2SO_4 injection mass per year, not the sulfur mass emitted per year. The most efficient alumina geoengineering scenario, with 240 nm monomers injected, has roughly the same RF efficiency per megaton of emissions as geoengineering by injection of H_2SO_4 . However, if a geoengineering methodology were to transport only sulfur to the stratosphere and create H_2SO_4 in situ, then sulfur geoengineering would be more efficient than alumina per megaton per year transported.

Longwave, or infrared (IR), heating in the stratosphere, particularly in the tropical lower stratosphere, is another potential risk of geoengineering. To estimate this effect, we¹ use the Rapid Radiative Transfer Model (RRTM) developed by Atmospheric and Environmental Research (Mlawer et al., 1997; Clough et al., 2005) to calculate infrared radiative heating rates and top of the atmosphere shortwave radiative forcing for mean cloud-free tropical atmospheric profiles with and without a uniform aerosol density of 1 cm^{-3} between 18 and 23 km. The longwave heating rates shown in Table 1 for alumina, diamond, and sulfate are generated by scaling the RRTM results for number densities of 1 cm^{-3} to the average number density in the 18–23 km region between 30° S and 30° N for scenarios predicted to produce -2 W m^{-2} of shortwave radiative forcing. For alumina and diamond, the RRTM calculation uses only the monomer size of 240 or 160 nm, respectively, ignoring fractal particles and treating coated monomers the same as uncoated monomers. For sulfate particles, we employ a size distribution due to the sensitivity of longwave heating rates to particle diameter and the range of diameters generated in geoengineering scenarios. We find that the longwave heating rate from alumina is approximately 4–5 times less than the heating rate from sulfate, comparing scenarios which each generate -2 W m^{-2} of RF, while longwave heating from diamond is minimal.

¹The RRTM calculations were performed by John Dykema.

3.5 Ozone impacts

Heterogeneous reactions on stratospheric particles play an important role in ozone chemistry by converting inactive forms of chlorine and bromine to forms that contribute directly to catalytic destruction of ozone. In addition, the heterogeneous conversion of N_2O_5 to HNO_3 reduces NO_x concentrations. This increases ozone concentrations in the middle stratosphere where NO_x reactions dominate the ozone loss cycles, but it decreases ozone concentrations in the lower stratosphere where HO_x , ClO_x , and BrO_x loss cycles dominate. Transient increases in sulfate aerosols following volcanic eruptions have caused temporary depletions in ozone (Solomon, 1999). Geoengineering by stratospheric aerosol injection would be expected to lead to analogous ozone depletion, depending on the heterogeneous reactions that occur on the particle surfaces and their rates.

Ozone loss due to geoengineering injections of sulfate precursors has been explored by several authors (Heckendorn et al., 2009; Tilmes et al., 2008, 2009). Here we provide a preliminary assessment of ozone loss from geoengineering injection of alumina and diamond solid particles. To enable comparison of the ozone impact of sulfate geoengineering we use the same model to compute change in ozone abundance arising from injections of both solid particles and of sulfate aerosols. We use the AER 2-D chemistry-transport-aerosol model which includes full ozone chemistry, with 50 transported species, an additional 51 radical species, 286 two- and three-body chemical reaction, 89 photolysis reactions, and 16 rainout/washout removal processes. Reaction rates are from the JPL compendium (Sander et al., 2011). The model parameterizes PSCs using thermodynamic equilibrium and includes sedimentation of ice and solid NAT particles. This model does not include radiative or dynamical feedbacks; temperature and circulation are fixed with a climatology averaged over the years 1978 through 2004. Thus our evaluation of ozone changes due to geoengineering by injection of solid particles includes only chemical perturbations due to heterogeneous reactions on

11819

particle surfaces and not due to changes in temperature or dynamics induced by the geoengineering.

The amount of ozone loss induced by stratospheric aerosols is strongly dependent on the concentrations of halogen species, Cl and Br. Concentrations of halogens are expected to decline as a result of emissions controls, so the impact of stratospheric aerosols on ozone will – all else being equal – decline over time. To err on the side of caution by overstating the ozone impacts, we use present-day trace gas concentration throughout this study with 3.4 ppbv of total chlorine and 23 pptv of total bromine, including 6 pptv of inorganic bromine derived from the very short lived organic compounds CH_2Br_2 and CHBr_3 . A more detailed evaluation of ozone impacts of solid particle geoengineering will await further studies with coupled aerosol-chemistry-climate models.

Aerosol surface area density (SAD) contributes to determining the rates of heterogeneous chemical reactions that occur on particle surfaces. Heterogeneous reactions may occur on bare alumina surfaces in the stratosphere, as well as on sulfate surfaces. The reaction $\text{ClONO}_2 + \text{HCl} \rightarrow \text{Cl}_2 + \text{HNO}_3$ has been measured on alumina surfaces (Molina et al., 1997; Sander et al., 2011) and would be expected to cause ozone depletion (Danilin et al., 2001; Jackman et al., 1998), though uncertainties in this reaction and the surface properties of alumina aerosol remain unexplored. Figure 8 shows bare alumina surface area density for the cases with 1 Mtyr^{-1} injection of 80 nm monomers (left panel) and 240 nm monomers (right panel). Alumina SAD is largest in the tropics where particles are injected, and is lower at higher latitudes where a larger fraction of the surfaces are coated with sulfate. Alumina SAD extends to higher altitudes, up to 40 km and above, with injection of 80 nm monomers, whereas the 240 nm monomers and their fractal derivatives sediment fast enough to preclude significant SAD above 30 km. Note that sulfate aerosols generally evaporate above about 35 km altitude, and thus geoengineering with solid particles may introduce significant surface area density in regions that currently are not greatly impacted by heterogeneous chemistry.

Figure 9 shows sulfate SAD from the calculated background atmosphere without geoengineering (panel a) and the increase in sulfate SAD in an atmosphere with

11820

1 Mtyr⁻¹ of geoengineering injection of 80 nm alumina monomers (panel b) or 240 nm alumina monomers (panel c). While the addition of alumina particles has produced only a small change in the total stratospheric condensed sulfate (see Fig. 5b), it has produced significant increases in sulfate surface area density. This is a result of sulfate being distributed in thin layers on the surfaces of alumina particles. With injection of 80 nm monomers, the sulfate SAD has increased by factors of 2–4, with maximum SAD at high latitudes. With injection of 240 nm monomers, the maximum sulfate SAD occurs in the tropics. Figure 9d shows the increase in sulfate SAD for a geoengineering scenario with 1 Mtyr⁻¹ of SO₂ injection as calculated by the AER 2-D model. The SAD increase is similar in magnitude to the case with injection of 80 nm alumina monomers, but has a distribution similar to the 240 nm alumina injection case. A similar injection of sulfur as H₂SO₄, as in Pierce et al. (2010), produces more than double this SAD increase. We would expect similar chemical ozone loss from similar changes in sulfate SAD whether due to geoengineering by SO₂, H₂SO₄, or alumina injection.

The SAD generated by alumina geoengineering is reduced when the monomer size of the injected particles increases. Optimizing the injected monomer size would be an important strategy to minimize stratospheric ozone depletion. Figure 10 illustrates this, showing annual averaged SAD between 15 and 25 km for bare alumina (panel a) and total sulfate (pure sulfate plus sulfate-coated alumina, panel b) as a function of emission rate with injections of 80, 160, 240, and 320 nm monomers. The SAD for bare alumina drops by factors of 1.8 to 3.1, depending on injection rate, when the monomer size is increased from 80 to 160 nm. The alumina SAD is roughly linear with emission rate, since the alumina surface area density does not decrease as particles coagulate when $D_h = 2.0$. The total sulfate SAD (Fig. 10b) is even more dependent on monomer diameter than is the alumina SAD. Even though the burden of stratospheric sulfate on alumina varies slowly with emission rate, the sulfate SAD varies rapidly with emission as the sulfate becomes spread more thinly over a greater numbers of alumina particles. The dashed lines in Fig. 10 represent cases where the coated particles take

11821

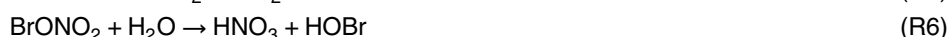
on a more compact fractal shape, and thus sediment faster, greatly decreasing sulfate SAD, especially for the 80 nm injection case.

Our model evaluation of ozone impacts from alumina geoengineering considers the following reaction on bare alumina surfaces:



This reaction, with reaction probability γ of 0.02, has been studied in relation to ozone depletion resulting from space shuttle launches (Danilin et al., 2001; Jackman et al., 1998). We assume that this reaction occurs catalytically with no surface poisoning. Other potential reactions on alumina surfaces have been investigated in the laboratory (see Sander et al., 2011), and further investigation is needed to determine how additional heterogeneous and photocatalytic reactions could modify stratospheric chemistry or change the surface properties of alumina in the stratosphere. Measurements of potential heterogeneous reactions on diamond surfaces are not available. Thus we perform diamond injection calculations assuming Reaction (R1) on diamond at the same rate as for alumina, and assuming no reactions on bare diamond surfaces.

We also consider heterogeneous reactions on the sulfate-coated surfaces of solid particles. These reactions include:



11822

Due to the solubility of HCl, ClONO₂, HOCl, and HOBr in sulfuric acid solutions, Reactions (R3)–(R5), and (R8) can be considered bulk processes or hybrid bulk–surface processes governed by a reaction–diffusion process. For liquid spherical particles we use standard methods to calculating the reaction probability as a function of radius (Shi et al., 2001). For reactions on coated solid particles, we use the same functions, substituting the thickness of the sulfate layer in place of the radius of a spherical particle.

Calculated changes in ozone due to heterogeneous reactions on alumina surfaces (bare alumina and sulfate-coated alumina) are shown in Fig. 11 for cases with injection of 80 and 240 nm monomers at an emission rate of 1 Mtyr^{−1}. Column ozone depletion ranges from 2 % in the tropics to 6–10 % at midlatitudes and up to 14 % at the poles in springtime with injection of 80 nm monomers. With injection of 240 nm monomers, ozone depletion is much smaller, ranging from 0.3 to 2.5 %. The annual average ozone change as a function of latitude and altitude (Fig. 11, right hand panels) shows features linked to ozone's formation rate, chemical destruction rate, and transport timescale. In the tropics, ozone concentrations are determined by the chemical production via UV radiation that is balanced by transport out of the tropics to higher latitudes. Thus ozone changes due to increased loss mechanisms are minimal in the tropics in the stratosphere, though increased penetration of UV to lower altitudes in the tropics can produce ozone increases. In the middle stratosphere, 25–35 km altitude, the NO_x cycle dominates ozone loss. Increases in aerosol surface area density in this region reduce NO and NO₂ while increasing HNO₃ via the N₂O₅ + H₂O reaction. Thus the NO_x loss cycle is diminished and ozone increases. The sedimentation rate of alumina particles is significant, as the scenario with injection of 80 nm monomers yields significant increases in aerosol surface area density and ozone changes above 25 km, whereas the scenario with 240 nm monomers injected does not. In the lower stratosphere at mid and high latitudes, the heterogeneous reactions on particle surfaces increase the ratio of chlorine and bromine in their radical forms that destroy ozone (Cl, ClO, Br, and BrO). In addition, the N₂O₅ + H₂O reaction leads to more HNO₃ and less ClONO₂ and BrONO₂, thus indirectly increasing halogen radicals as well. Local ozone depletions in

11823

the lower stratosphere are as large as 24 % with 80 nm monomer injections and 5 % with 240 nm monomer injections, on an annual average basis.

Figure 12a shows annual average changes in ozone column as a function of latitude with 1 Mtyr^{−1} of geoengineering alumina emissions. Results with injection of 80, 160, and 240 nm monomers are shown. We don't calculate ozone changes due to injection of 320 nm monomers because these scenarios produce less radiative forcing than injection of 240 nm monomers for similar emission rates. Ozone changes, similar to SAD increases, are found to be very sensitive to injected monomer size. However, assuming that coated alumina particles assume a more compact shape (shown by dashed lines in the figure) significantly reduces calculated ozone depletion for the $R_0 = 80$ nm case, and modestly reduces ozone depletion for the $R_0 = 160$ nm case. Figure 12b shows calculated ozone changes for emission rates of 1, 2, 4, and 8 Mtyr^{−1} with injection of 240 nm alumina monomers. Note that ozone changes increase at a less than linear rate with increasing emissions, and that the effect of compaction of coated alumina particles becomes more significant at higher emission rates due to formation of higher-order fractals. Figure 12c shows calculated ozone changes due to geoengineering emission of diamond monomers of 160 nm radius. Solid lines are for results including the Reaction (R1) on uncoated particles, and dotted lines omit this reaction. Reaction (R1) has a greater effect in the tropics than at mid latitudes due to higher concentrations of uncoated particles there. The northern high latitudes show greater sensitivity to geoengineering emissions than the southern high latitudes at the higher emission levels, likely due to the dominant role of PSCs over the Antarctic.

Global average column ozone changes are shown in Fig. 13a as functions of injected monomer size and emission rate. Figure 13b shows changes in global average ozone as a function of the associated radiative forcing for each scenario. This makes it clear that geoengineering injection of 80 nm alumina monomers is completely unworkable, producing excessive ozone depletion (5 % with 1 Mtyr^{−1} injection and 14 % with 8 Mtyr^{−1} injection) and minimal radiative forcing. Geoengineering by injection of 240 nm alumina monomers, however, could potentially be an effective climate control

11824

strategy, similar to geoengineering by injection of sulfur in its radiative forcing effectiveness but with less ozone depletion potential. Note that radiative forcing and associated ozone depletion with 16 Mtyr^{-1} injection of 240 nm alumina monomers is included in the Fig. 13b, yielding almost 4 W m^{-2} of RF with about 8 % ozone depletion. Injection of 160 nm diamond monomers produces ozone loss per megaton of injection similar to 160 nm alumina monomers, but with radiative forcing per megaton of injection greater than for similar injections of 240 nm alumina monomers. We show diamond results both including and excluding Reaction (R1) on bare diamond surfaces. This reaction makes about a 10–15 % difference in ozone depletion due to diamond injection. Note that the SO_2 results plotted in Fig. 13 show more ozone depletion than in Heckendorn et al. (2009) because that study did not include the short-lived bromine source gases. More studies will be needed to evaluate potential impacts on stratospheric chemistry such as tropopause heating and changes in the Brewer–Dobson circulation that are not evaluated here.

4 Discussion

We have developed a new aerosol model and used it to quantitatively explore the interactions of solid particles with sulfate aerosol in the stratosphere. This analysis allows a preliminary assessment of some of the trade-offs that might arise in using solid aerosols such as alumina or diamond rather than sulfates for solar geoengineering. We first discuss salient limitations of our model before turning to analysis of trade-offs.

4.1 Limitations

4.1.1 Injection mechanism

We do not model the mechanism for injection and dispersion of aerosols. If aerosols were injected from aircraft there would be small-scale dynamical effects in the injection nozzle and in the aircraft plume in which particle concentrations would be much larger

11825

than found after dilution to the scale of a model grid box, possibly leading to rapid coagulation. Effects during particle generation or injection from a nozzle would occur on very short time and space scales and cannot be estimated here. We can, however, estimate the impact of coagulation in an expanding plume using the method of Pierce et al. (2010). We allow the plume cross-section to dilute from 6 m^2 to $17 \times 10^6 \text{ m}^2$ over a 48 h period, assuming that alumina particles are released at a rate of 30 kg km^{-1} of flight path. We find the fraction of alumina mass remaining as monomers after 48 h of plume dilution to be 37, 86, 96, and 98 % for injected monomers of 80, 160, 240, and 320 nm, respectively. For monomer injections of 240 and 320 nm, only 2-monomer fractals are created within 48 h. We conclude that plume dynamics and processing are unlikely to have a substantial effect on alumina geoengineering if injected monomer size is greater than 160 nm. For 240 nm monomer, the most relevant case, our 2-D model calculation would be expected to have 4 % less mass in monomers if plume dynamics were considered.

4.1.2 Two-dimensional model

A second limitation is the use of a 2-D model. Since the geoengineering scenarios discussed in this work deal with particle injection in the 20–25 km altitude region and spread between 30° S and 30° N , assuming zonal symmetry, as a 2-D model implicitly does, does not detract greatly from the validity of our results. In particular, if the method of injecting alumina particles attempts to distribute them uniformly in space and time and avoid overlapping emissions as much as possible, then a zonally-symmetric spread may be a fairly good approximation. However, details of transport near and below the tropopause are not well-represented in 2-D models. Thus a 3-D model would be needed to accurately represent this region. And if a specific geoengineering injection methodology were to be investigated, a 3-D model with fine resolution would be needed to examine heterogeneities in the resulting aerosol distribution.

4.1.3 Geometry of aggregates

The fractal geometry of aggregates likely depends on the formation mechanism, and it is plausible that the actual fractal dimensions might differ significantly from the D_f value of 1.6 we use here for alumina and diamond. While the fractal dimension of alumina has been measured for monomer cores much smaller than considered here, that of diamond has not. It is also plausible that variables k_f and k_h should have values other than 1.0, at least for cases that calculate many high-order fractals. The behavior of aggregates under stratospheric conditions has not been studied extensively. The formulations we have adopted for coagulation, condensation, and sedimentation are based on theoretical studies or on tropospheric or liquid-medium experiments, and thus should be considered uncertain. Our assumption of maximal compaction instantaneously on wetting is likely not realistic but meant to show the greatest possible affect of potential particle compaction on aging. Observational studies in the laboratory and in the stratosphere would be needed to determine whether compaction of alumina particles occurs and to what extent. However, compaction has a minor effect on the radiative properties and ozone depletion potential of particles with monomer sizes of ~ 200 nm or greater.

4.1.4 Ozone chemistry

The surface chemistry of alumina and other solid particles potentially useful for geo-engineering has not been studied as extensively as that of sulfate particles. We include only one reaction, $\text{ClONO}_2 + \text{HCl}$, on alumina and diamond particles in this modeling study. Laboratory studies have investigated some additional reactions on alumina surfaces, and there may be others not yet explored. Reported reactions on Al_2O_3 surfaces include the uptake of NO_2 and HNO_3 and reactions of several volatile organic compounds, including formaldehyde, methanol, and acetic acid (Sander et al., 2011). In addition, photocatalysis reactions of several species on Al_2O_3 surfaces have been reported (de Richter and Caillol, 2011), and may depend on the exact composition or impurities of the particle surface. Photocatalysis of CFC compounds has been con-

11827

sidered as a method to mitigate the atmospheric burden of greenhouse gases if augmented by artificial UV radiation in the troposphere. However, if these reactions were effective in the stratosphere, they would contribute to the formation of free radical chlorine and bromine, possibly increasing ozone depletion while reducing the lifetime the CFCs. Studies of these and other reactions under stratospheric photochemical conditions would need to be performed on any solid particle under consideration for geo-engineering application.

4.1.5 Missing feedbacks

The modeling we present is missing a number of feedback processes that may be important in the atmosphere and may significantly change the radiative forcing or ozone depletion estimates given here. These include changes in stratospheric temperature due to aerosol heating, which would modify rates of reactions important to ozone formation and loss. Aerosol heating and enhanced equator-pole temperature gradients would also modify the strength of the Brewer–Dobson circulation and the polar vortex, with impacts on aerosol concentration, PSC formation, and ozone concentration. Increases in the temperature of the tropical tropopause layer would increase the transport of water vapor across the tropopause, increasing stratospheric H_2O and OH concentrations, and reducing ozone (Heckendorn et al., 2009). These additional ozone changes would further modify stratospheric temperature and circulation. A more uncertain feedback process is the effect of enhanced aerosol concentrations on upper tropospheric cloudiness and cloud radiative properties (Cirisan et al., 2013). A general circulation model with stratospheric chemistry and aerosol and cloud microphysics would be needed to evaluate these feedback effects.

4.2 Principal findings

Use of alumina particles for SRM is potentially useful only if the size of the injected monomers is larger than about 150 nm; the best results are only seen if the monomer

radius exceeds about 200 nm. The strong dependence on monomer size can be understood if one assumes that the injection rate will be adjusted so as to produce a given radiative forcing, for example 2 W m^{-2} . For alumina, the peak mass-specific upscattering efficiency occurs at a radius of $\sim 200 \text{ nm}$. As the monomer size gets smaller
 5 a higher monomer density and mass injection rate is required to maintain the specified radiative forcing. The coagulation rate increases as the square of monomer density, so the fraction of monomers in aggregates increase rapidly with monomer density. Finally, the mass-specific radiative forcing for aggregates decreases quickly with the number of monomers in an aggregate, so the injection rate must be increased further to maintain
 10 a fixed radiative forcing. The net effect is that the radiative efficacy, the global radiative forcing per unit mass injection rate, declines very rapidly for particle radii below 150 nm. We find that alumina monomers with radii of roughly 240 nm provide the most radiative forcing for a given injection rate. For particle sizes beyond 240 nm, the scattering efficiency remains roughly constant while the sedimentation rate increases, contributing
 15 to a decrease in radiative forcing efficiency per unit injection rate.

As a specific example, consider the injection of 240 nm monomers at a rate of 4 Mt yr^{-1} evenly distributed between 30° S to 30° N and from 20–25 km in altitude. This produces a stratospheric burden of 4.6 Mt and global radiative forcing of 1.3 W m^{-2} . Under these conditions, coagulation of alumina particles is minimal: 81 % of the alumina is
 20 in monomers and only 4 % is in aggregates of more than two monomers. Particle densities are a maximum in the lower stratosphere with peak concentrations of $1\text{--}7 \text{ cm}^{-3}$. The net effect of interaction with the background stratospheric sulfate is that about 50 % of the stratospheric sulfate is found as a coating with a typical depth of order 10 nm on the alumina particles. The total sulfate burden is reduced from 0.11 to 0.08 Mt because
 25 the relatively fast fall speeds of the alumina aerosol provide a sedimentation sink for sulfates, yet the sulfate surface area density is increased by $1\text{--}3.5 \mu\text{m}^2 \text{ cm}^{-3}$ in the lower stratosphere.

This perturbation decreases column ozone by 3.6 % with maximum ozone loss of 4 to 7 % over polar regions. As with sulfate aerosols, ozone concentrations increase

11829

at altitudes around 30 km in the mid stratosphere where the NO_x cycle dominates but this is more than compensated by the halogen-catalyzed ozone loss in the lower stratosphere. And with injection of 240 nm monomers, sedimentation is rapid enough to preclude significant aerosol concentrations above 25–30 km. Most of the ozone impact
 5 of alumina aerosols is found to be due the increase in sulfate surface area and heterogeneous reactions on the liquid sulfuric acid. This is because most of the alumina particles are coated with sulfate at mid and high latitudes where ozone loss reactions largely determine the ozone concentration. If the rate of Reaction (R1) is set to zero in our simulations, the column ozone depletion changes by less than 15 % in the extra-
 10 tropics, but up to 35 % in the tropics. Thus uncertainty in the rate of Reaction (R1) or the nature of the uncoated alumina surface does not have a strong influence on our calculated ozone impacts. If we assume that the alumina particle surfaces remain uncoated and that Reaction (R1) occurs on all alumina particles, we find that the ozone depletion is much less than that obtained when the surfaces do become coated, implying that Reaction (R1) on alumina surfaces has less effect on ozone than do sulfate
 15 heterogeneous reactions on the same surface area, mostly due to the effectiveness of heterogeneous bromine reactions.

We can achieve a similar radiative forcing of 1.3 W m^{-2} with injection of 160 nm radius diamond monomers at 2 Mt yr^{-1} . This emission rate produces a stratospheric burden
 20 of 3.3 Mt of diamond. The corresponding ozone depletion due to diamond injection ranges between 3.8 % globally due to increased sulfate surface area alone to 4.3 % when we assume that Reaction (R1) occurs on the bare surface of diamond particles with the same reaction rate employed for alumina. However, levels of ozone depletion are highly uncertain as this reaction, and other potential heterogeneous reactions on
 25 diamond surfaces, have not been measured.

4.3 Comparison with sulfate aerosols

Whatever method is used to create an artificial radiative forcing, solar geoengineering is – at best – an imperfect method for reducing climate impacts. Any technology

11830

for producing radiative forcing will have a set of *technology-specific impacts*, such as ozone loss arising from the introduction of aerosol particles into the stratosphere. However the radiative forcing is produced, the *efficacy* of SRM is inherently limited by the fact that a change in solar radiative forcing cannot perfectly compensate for the radiative forcing caused by increasing greenhouse gases (Kravitz et al., 2014; Curry et al., 2014). A central motivation for considering solid aerosols rather than sulfates is that they might have less severe technology-specific risks. As discussed in the introduction, the principle technology-specific risks or side-effects of sulfate aerosols are ozone loss, increased diffuse light, and stratospheric heating.

Loss of stratospheric ozone and an increase in diffuse light have direct impacts on ecosystems and human health. The consequences of stratospheric heating are indirect and more speculative. Heating of the tropical tropopause layer (TTL) might be expected to increase the amount of water vapor entering the stratosphere. An increase in TTL temperature of 1 K increases the concentration of water vapor entering the stratosphere by about 0.8 ppmv (Kirk-Davidoff, 1999). Geoengineering with sulfate aerosols might heat the TTL region by several degrees, increasing stratospheric water vapor concentrations by more than 2 ppmv (Heckendorn et al., 2009). This would in turn exacerbate ozone loss and create a positive radiative forcing that would offset some of the reduction in forcing from SRM. While there is uncertainty about the exact consequences of heating the lower stratosphere, it's reasonably certain that all-else-equal, a geoengineering method that does not heat the low stratosphere is preferable to one that does.

We estimate stratospheric heating for alumina, diamond, and sulfate geoengineering scenarios with the RRTM model, as described in Sect. 3.4. Our results for alumina are broadly consistent with the results of Ferraro et al. (2011) for titania. Note, however, that Ross and Shaeffer (2014) conclude that the positive infrared radiative forcing from alumina can be larger than the negative radiative forcing from solar scattering by the same particles. We suspect that part of this discrepancy comes from the fact that Ferraro et al. (2011) and this paper assume a narrow size distribution close to the optimal for solar scattering, whereas Ross and Shaeffer (2004) use a broad alumina size dis-

11831

tribution. However, we have not resolved this discrepancy, so our estimate of heating for alumina should be taken as uncertain.

As shown in Table 1, our results suggest that alumina may have less severe technology-specific risks than sulfates. While the injected mass necessary to achieve a -2 W m^{-2} radiative forcing is roughly equivalent whether employing alumina or sulfate aerosol, the ozone depletion is more severe with sulfate geoengineering. In addition, the increase in diffuse solar radiation would be half as much with alumina as with sulfate, and the stratospheric heating is expected to be considerably less, smaller by a factor of 4–5 in our estimation. Diamond appears to offer excellent shortwave scattering with only a small increase in diffuse light. We estimate ozone depletion due to diamond to be less than that due to sulfate, but uncertainty is large. Longwave absorption from diamond is insignificant.

We conclude that SRM by injection of solid particles may have some advantages relative to sulfates and merits further study to reduce the sizable uncertainties that currently exist. It is important to note that the injection of substances like alumina or diamond nanoparticles have much greater “unknown unknowns” than sulfates, as they would be novel substances in the stratosphere. Laboratory studies of reaction kinetics for these particles under stratospheric conditions, as well as studies of their microphysical and radiative properties, are required to reduce uncertainties.

Author contributions. D. Keith conceived this study and provided overall scientific direction. D. Weisenstein developed the solid–liquid aerosol model and performed the 2-D calculations, while D. Keith performed the shortwave radiative calculations. Both authors contributed substantially to manuscript preparation.

Acknowledgements. Funding for this study provided by a grant from the Fund for Innovative Climate and Energy Research (FICER). The authors would like to thank John Dykema for assistance with longwave heating calculations, and Frank Keutsch and Sebastian Eastham for insightful comments on earlier drafts of this paper.

11832

References

- Blackstock, J. J., Battisti, D. S., Caldeira, K., Eardley, D. M., Katz, J. I., Keith, D. W., Patri-
nos, A. A. N., Schrag, D. P., Socolow, R. H., and Koonin, S. E.: Climate Engineering Re-
sponses to Climate Emergencies, Novim, available at: <http://arxiv.org/pdf/0907.5140> (last
5 access: 16 April 2015), 2009.
- Brock, C. A., Hamill, P., Wilson, J. C., Jonsson, H. H., Chang, K. R.: Particle formation in the
upper tropical troposphere: a source of nuclei for the stratospheric aerosol, *Science*, 270,
1650–1653, 1995.
- Cirisan, A., Spichtinger, P., Luo, B. P., Weisenstein, D. K., Wernli, H., Lohmann, U., and Peter, T.:
10 Microphysical and radiative changes in cirrus clouds by geoengineering the stratosphere, *J.*
Geophys. Res., 118, 4533–4548, doi:10.1002/jgrd.50388, 2013.
- Clough, S. A., Shephard, M. W., Mlawer, E. J., Delamere, J. S., Iacono, M. J., Cady-Pereira, K.,
Boukabara, S., and Brown, P. D.: Atmospheric radiative transfer modeling: a summary of the
AER codes, *J. Quant. Spectrosc. Ra.*, 91, 233–244, 2005.
- 15 Curry, C. L., Sillmann, J., Bronaugh, D., Alterskjaer, K., Cole, J. N. S., Ji, D., Kravitz, B., Krist-
jansson, J. E., Moore, J. C., Muri, H., Niemeier, U., Robock, A., Tilmes, S., and Yang, S.:
A multimodel examination of climate extremes in an idealized geoengineering experiment, *J.*
Geophys. Res., 119, 3900–3923, doi:10.1002/2013JD020648, 2014.
- Danilin, M. Y., Shia, R.-L., Ko, M. K. W., Weisenstein, D. K., Sze, N. D., Lamb, J. J., Smith, T. W.,
20 Lohn, P. D., and Prather, M. J.: Global stratospheric effects of the alumina emissions by solid-
fueled rocket motors, *J. Geophys. Res.*, 106, 12727–12738, 2001.
- De Richter, R. and Caillol, S.: Fighting global warming: the potential of photocatalysis against
CO₂, CH₄, N₂O, CFCs, tropospheric O₃, BC and other major contributors to climate
change, *J. Photoch. Photobio. C*, 12, 1–19, doi:10.1016/j.jphotochemrev.2011.05.002, 2011.
- 25 Dvortsov, V. L., Geller, M. A., Yudin, V. A., and Smyshlyayev, S. P.: Parameterization of
the convective transport in a two-dimensional chemistry-transport model and its valida-
tion with radon 222 and other tracer simulations, *J. Geophys. Res.*, 103, 22047–22062,
doi:10.1029/98JD02084, 1998.
- Ferraro, A. J., Highwood, E. J., and Charlton-Oerez, A. J.: Stratospheric heating by poten-
30 tial geoengineering aerosols, *Geophys. Res. Lett.*, 38, L24706, doi:10.1029/2011GL049761,
2011.

11833

- Filippov, A. V., Zurita, M., and Rosner, D. E.: Fractal-like aggregates: relation between morphol-
ogy and physical properties, *J. Colloid Interf. Sci.*, 229, 261–273, 2000.
- Fleming, E. L., Jackman, C. H., Stolarski, R. S., and Considine, D. B.: Simulation of strato-
spheric tracers using an improved empirically-based two-dimensional model transport for-
5 mulation, *J. Geophys. Res.*, 104, 23911–23934, 1999.
- Hamill, P., Jensen, E. J., Russell, P. B., and Bauman, J. J.: The life cycle of stratospheric aerosol
particles, *B. Am. Meteorol. Soc.*, 78, 1395–1410, 1997.
- Heckendorn, P., Weisenstein, D., Fueglistaler, S., Luo, B. P., Rozanov, E., Schraner, M., Thoma-
son, L. W., and Peter, T.: The impact of geoengineering aerosols on stratospheric tempera-
10 ture and ozone, *Environ. Res. Lett.*, 4, 045108, doi:10.1088/1748-9326/4/4/045108, 2009.
- Hinklin, T., Toury, B., Gervais, C., Babonneau, F., Gislason, J. J., Morton, R. W., and
Laine, R. M.: Liquid-feed flame spray pyrolysis of metalloorganic and inorganic alu-
mina sources in the production of nanoalumina powders, *Chem. Mater.*, 16, 21–30,
doi:10.1021/cm021782t, 2004.
- 15 Jackman, C. H., Considine, D. B., and Fleming, E. L.: A global modeling study of solid rocket
aluminum oxide emission effects on stratospheric ozone, *Geophys. Res. Lett.*, 25, 907–910,
1998.
- Johnson, C. P., Li, X., and Logan, B. E.: Settling velocities of fractal aggregates, *Environ. Sci.*
Technol., 30, 1911–1918, 1996.
- 20 Kajino, M. and Kondo, Y.: EMTACS: development and regional-scale simulation of a size, chem-
ical, mixing type, and soot shape resolved atmospheric particle model, *J. Geophys. Res.*,
116, D02303, doi:10.1029/2010JD015030, 2011.
- Karasev, V. V., Onischuk, A. A., Glotov, O. G., Baklinov, A. M., Zarko, V. E., and Panfilov, V. N.:
Charges and fractal properties of nanoparticles – combustion products of aluminum agglom-
25 erates, *Combust. Explo. Shock+*, 37, 734–736, 2001.
- Karasev, V. V., Onischuk, A. A., Glotov, O. G., Baklanov, A. M., Maryasov, A. G., Zarko, V. E.,
Panfilov, V. N., Levykin, A. I., and Sabelfeld, K. K.: Formation of charged aggregates of
Al₂O₃ nanoparticles by combustion of aluminum droplets in air, *Combust. Flame*, 138, 40–54,
2004.
- 30 Keith, D. W.: Photophoretic levitation of engineered aerosols for geoengineering, *P. Natl. Acad.*
Sci. USA, 107, 16428–16431, doi:10.1073/pnas.1009519107, 2010.

11834

- Kirk-Davidoff, D. B., Hints, E. J., Anderson, J. G., and Keith, D. W.: The effect of climate change on ozone depletion through changes in stratospheric water vapour, *Nature*, 402, 399–401, 1999.
- Kravitz, B., MacMartin, D. G., and Caldeira, K.: Geoengineering: whiter skies?, *Geophys. Res. Lett.*, 39, L11801, doi:10.1029/2012GL051652, 2012.
- 5 Kravitz, B., MacMartin, D. G., Robock, A., Rasch, P. J., Ricke, K. L., Cole, J. N. S., Curry, C. L., Irvine, P. J., Ji, D., Keith, D. W., Kristjansson, J. E., Moore, J. C., Muri, H., Singh, B., Tilmes, S., Watanabe, S., Yang, S., and Yoon, J.-H.: A multi-model assessment of regional climate disparities caused by solar geoengineering, *Environ. Res. Lett.*, 9, 074013, doi:10.1088/1748-9326/9/7/074013, 2014.
- 10 Krueger, A.: Diamond nanoparticles: jewels for chemistry and physics, *Adv. Mater.*, 20, 2445–2449, doi:10.1002/adma.200701856, 2008.
- Lawrence, C. R. and Neff, J. C.: The contemporary physical and chemical flux of aeolian dust: a synthesis of direct measurements of dust deposition, *Chem. Geol.*, 267, 46063, doi:10.1016/j.chemgeo.2009.02.005, 2009.
- 15 Maricq, M. M.: Coagulation dynamics of fractal-like soot aggregates, *J. Aerosol Sci.*, 38, 141–156, 2007.
- Maricq, M. M. and Nu, N.: The effective density and fractal dimension of soot particles from premixed flames and motor vehicle exhaust, *J. Aerosol Sci.*, 35, 1251–1274, 2004.
- 20 McClellan, J., Keith, D. W., and Apt, J.: Cost analysis of stratospheric albedo modification delivery systems, *Environ. Res. Lett.*, 7, 034019, doi:10.1088/1748-9326/7/3/034019, 2012.
- Mikhailov, E. F., Vlasenko, S. S., Podgorny, I. A., Ramanathan, V., and Corrigan, C. E.: Optical properties of soot-water drop agglomerates: an experimental study, *J. Geophys. Res.*, 111, D07209, doi:10.1029/2005JD006389, 2006.
- 25 Mlawer, E. J., Taubman, S. J., Brown, P. D., Iacono, M. J., and Clough, S. A.: RRTM, a validated correlated-k model for the longwave, *J. Geophys. Res.*, 102, 16663–16682, 1997.
- Molina, M. J., Molina, L. T., Zhang, R., Meads, R. F., and Spencer, D. D.: The reaction of ClONO₂ with HCl on aluminum oxide, *Geophys. Res. Lett.*, 24, 1619–1622, doi:10.1029/97GL01560, 1997.
- 30 Moreno-Cruz, J., Ricke, K., and Keith, D. W.: A simple model to account for regional inequalities in the effectiveness of solar radiation management, *Climatic Change*, 110, 649–668, doi:10.1007/s10584-011-0103-z, 2011.

11835

- Niemeier, U., Schmidt, H., and Timmreck, C.: The dependency of geoengineered sulfate aerosol on the emission strategy, *Atmos. Sci. Lett.*, 12, 189–194, doi:10.1002/asl.304, 2011.
- Pierce, J. R., Weisenstein, D. K., Heckendorn, P., Peter, T., and Keith, D. W.: Efficient formation of stratospheric aerosol for climate engineering by emission of condensable vapor from aircraft, *Geophys. Res. Lett.*, 37, L18805, doi:10.1029/2010GL043975, 2010.
- 5 Pitari, G., Aquila, V., Kravitz, B., Robock, A., Watanabe, S., Cionni, I., De Luca, N., Di Genova, G., Mancini, E., and Tilmes, S.: Stratospheric ozone response to sulfate geoengineering: results from the Geoengineering Model Intercomparison Project (GeoMIP), *J. Geophys. Res.*, 119, 2629–2653, doi:10.1002/2013JD020566, 2014.
- 10 Pope, F. D., Braesicke, P., Grainger, R. G., Kalberer, M., Watson, I. M., Davidson, P. J., and Cox, R. A.: Stratospheric aerosol particles and solar-radiation management, *Nature Climate Change*, 2, 713–719, doi:10.1038/NCLIMATE1528, 2012.
- Rannou, P., McKay, C. P., Botet, R., and Cabane, M.: Semi-empirical model of absorption and scattering by isotropic fractal aggregates of spheres, *Planet. Space Sci.*, 47, 385–396, 1999.
- 15 Rasch, P. J., Crutzen, P. J., and Coleman, D. B.: Exploring the geoengineering of climate using stratospheric sulfate aerosols: the role of particle size, *Geophys. Res. Lett.*, 35, L02809, doi:10.1029/2007GL032179, 2008.
- Ross, M. N. and Shaeffer, P. M.: Radiative forcing caused by rocket engine emissions, *Earth's Future*, 2, 177–196, doi:10.1002/2013EF000160, 2014.
- 20 Sander, S. P., Friedl, R. R., Barker, J. R., Golden, D. M., Kurylo, M. J., Wine, P. H., Abbatt, J. P. D., Burkholder, J. B., Kolb, C. E., Moortgat, G. K., Huie, R. E., and Orkin, V. L.: Chemical kinetics and photochemical data for use in atmospheric studies, Evaluation No. 17, JPL Publication 10-6, 2011.
- Shrand, A. M., Huang, H., Carlson, C., Schlager, J. J., Osawa, E., Hussain, S. M., and Dai, L.: Are diamond nanoparticles cytotoxic?, *J. Phys. Chem. B*, 111, 2–7, doi:10.1021/jp066387v, 2007.
- 25 Seinfeld, J. H. and Pandis, S. N.: *Atmospheric Chemistry and Physics*, John Wiley and Sons, Inc., 2006.
- Shi, Q., Jayne, J. T., Kolb, C. E., Worsnop, D. R., and Davidovits, P.: Kinetic model for reaction of ClONO₂ with H₂O and HCl and HOCl with HCl in sulfuric acid solutions, *J. Geophys. Res.*, 106, 24259–24274, 2001.
- 30 Solomon, S.: Stratospheric ozone depletion: a review of concepts and history, *Rev. Geophys.*, 37, 275–316, doi:10.1029/1999RG900008, 1999.

11836

- SPARC: SPARC Report No. 4, Assessment of Stratospheric Aerosol Properties (ASAP), WCRP-124 WMO/TD No. 1295, SPARC Report No. 4, edited by: Thomason, L. and Peter, T., WMO, 2006.
- Tabazadeh, A., Toon, O. B., Cleg, S. L., and Hamill, P.: A new parameterization of $\text{H}_2\text{SO}_4/\text{H}_2\text{O}$ aerosol composition: atmospheric implications, *Geophys. Res. Lett.*, 24, 1931–1934, 1997.
- Teller, E., Wood, L., and Hyde, R.: Global Warming and Ice Ages: I. Prospects for Physics-Based Modulation of Global Change, Lawrence Livermore National Laboratory Publication UCRL-JC-128715, 18 pp., 1997.
- Tilmes, S., Muller, R., and Salawitch, R.: The sensitivity of polar ozone depletion to proposed geoengineering schemes, *Science*, 320, 1201–1204, doi:10.1126/science.1153966, 2008.
- Tilmes, S., Garcia, R. R., Kinnison, D. E., Gettelman, A., and Rasch, P. J.: Impact of geo-engineered aerosols on the troposphere and stratosphere, *J. Geophys. Res.*, 114, D12305, doi:10.1029/2008JD011420, 2009.
- Tsuzuki, T. and McCormick, P. G.: Mechanochemical synthesis of nano particles, *J. Mater. Sci.*, 39, 5143–5146, 2004.
- US Geological Survey (USGS): 2012 Minerals Yearbook: Bauxite and Alumina, US Department of the Interior, Washington, D.C., available at: <http://minerals.usgs.gov/minerals/pubs/commodity/bauxite/myb1-2012-bauxi.pdf> (last access: 16 April 2015), 2014.
- Weisenstein, D. K., Yue, G. K., Ko, M. K. W., Sze, N.-D., Rodriguez, J. M., and Scott, C. J.: A two-dimensional model of sulfur species and aerosols, *J. Geophys. Res.*, 102, 13019–13035, 1997.
- Weisenstein, D. K., Eluszkiewicz, J., Ko, M. K. W., Scott, C. J., Jackman, C. H., Fleming, E. L., Considine, D. B., Kinnison, D. E., Connell, P. S., and Rotman, D. A.: Separating chemistry and transport effects in 2-D models, *J. Geophys. Res.*, 109, D18310, doi:10.1029/2004JD004744, 2004.
- Weisenstein, D. K., Penner, J. E., Herzog, M., and Liu, X.: Global 2-D intercomparison of sectional and modal aerosol modules, *Atmos. Chem. Phys.*, 7, 2339–2355, doi:10.5194/acp-7-2339-2007, 2007.
- Wilton, D. J., Hewitt, C. N., and Beerling, D. J.: Simulated effects of changes in direct and diffuse radiation on canopy scale isoprene emissions from vegetation following volcanic eruptions, *Atmos. Chem. Phys.*, 11, 11723–11731, doi:10.5194/acp-11-11723-2011, 2011.

11837

Table 1. Comparison of alumina, diamond, and sulfate solar geoengineering, based on a radiative forcing of -2 W m^{-2} for each case.

Metric	Alumina 240 nm	Diamond 160 nm	Sulfate as H_2SO_4	Sulfate as SO_2	Comments
Radiative forcing per unit injected mass flux ($\text{W m}^{-2} (\text{Mtyr}^{-1})^{-1}$)	-0.29	-0.50	-0.29 ^a	-0.22 ^a	Other than diamond, the differences are minor.
Ozone impact (global average column change)	-5 %	-6 to -7 % ^b	-13 % ^c	-10 % ^c	Alumina and diamond have less ozone depletion than sulfates, though there is considerable uncertainty.
Diffuse light increase (W m^{-2})	9.2	5.7	18	16	Alumina and diamond are both better (less diffuse light) than sulfates. Exact results would require a more sophisticated radiative transfer model.
Heating rate (K day^{-1}) in tropical lower stratosphere	0.033	< 0.001	0.16	0.13	Alumina is probably better (less heating) than sulfates, but this estimate is subject to considerable uncertainty. Diamond is much better.

^a Sulfate emission fluxes based on mass of H_2SO_4 and SO_2 emitted annually.

^b The results for diamond are a range based on two cases, with and without Reaction (R1) occurring on bare diamond surfaces.

^c Note that the overall ozone loss from H_2SO_4 and SO_2 injection is higher than reported in most previous studies because we consider short-lived bromine species.

11838

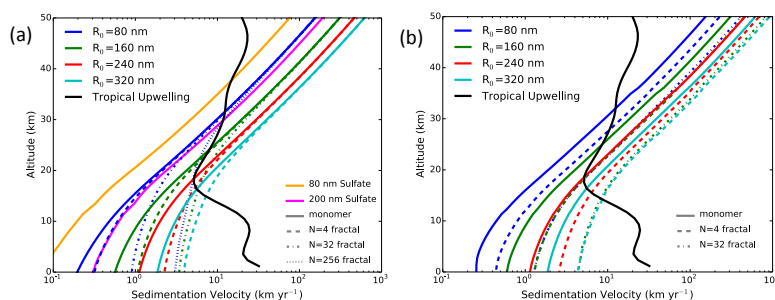


Figure 1. Sedimentation velocity (km yr⁻¹) vs. altitude for **(a)** uncoated alumina particles and pure sulfate particles and **(b)** sulfate-coated aged alumina with compact fractal structures. Solid colored lines represent monomers, dashed lines fractals with $N = 4$, dash-dot lines fractals with $N = 32$, and dotted lines fractals with $N = 256$ (for $R_0 = 80$ nm only). Fractal dimension $D_f = 1.6$ for uncoated particles represented in **(a)**, $D_f = 2.8$ for coated and compacted particles shown in **(b)**. The black lines represent the average upwelling velocity of the model's advective transport averaged over the region from 20° S to 20° N latitude for comparison.

11839

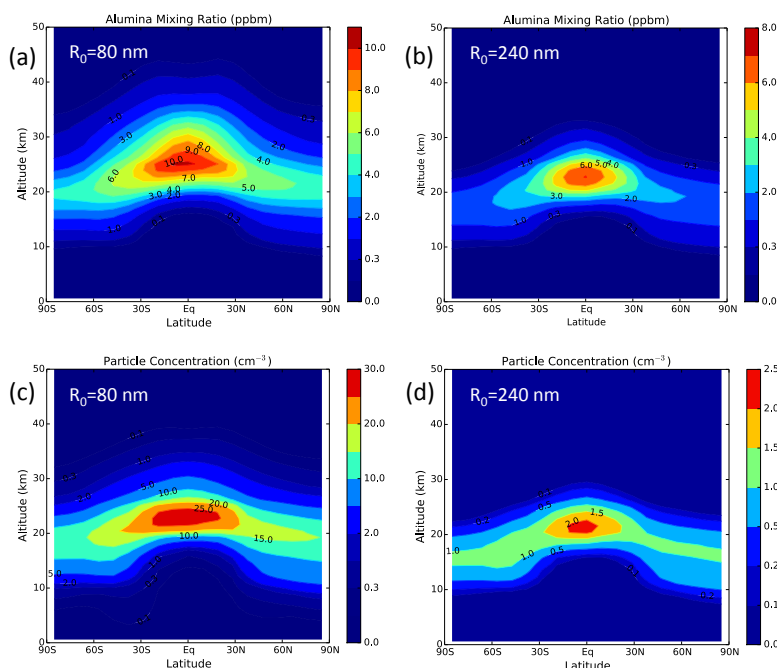


Figure 2. Concentration of alumina in ppbm **(a and b)** and number density of alumina particles in cm⁻³ **(c and d)** with geoengineering injections of 1 Mt yr⁻¹ of 80 nm monomers **(a and c)** and 1 Mt yr⁻¹ of 240 nm monomers **(b and d)**.

11840

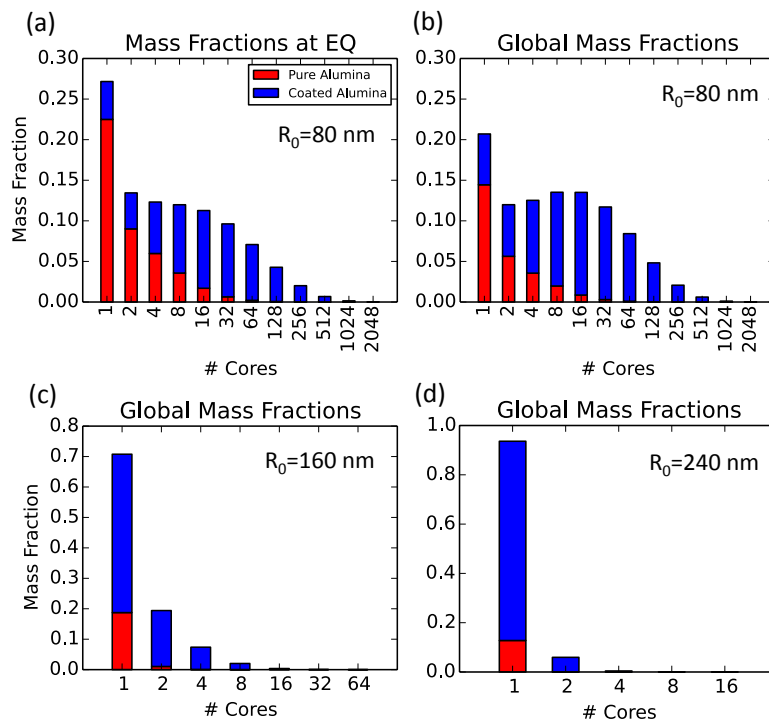


Figure 3. Distribution of integrated stratospheric alumina mass into monomers and fractals for geoengineering injection of 1 Mt yr^{-1} of alumina as 80 nm monomers at (a) the equator and (b) globally integrated, and for injection of 1 Mt yr^{-1} of alumina as (c) 160 and (d) 240 nm monomers globally integrated. Red bar length represents the mass fraction in dry alumina and blue bar length the mass fraction in coated alumina.

11841

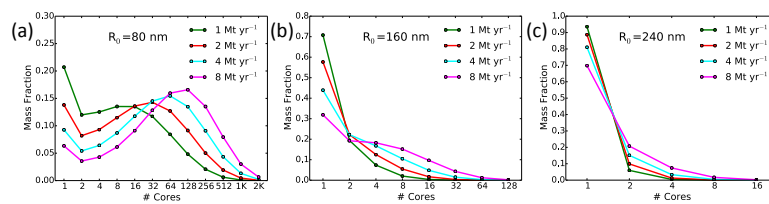


Figure 4. Calculated annual average stratospheric mass fractions of alumina as a function of the number of monomers contained in a fractal particle for (a) monomer injections of 80 nm radius, (b) monomer injections of 160 nm , and (c) monomer injections of 240 nm radius, with emission rates ranging from 1 to 8 Mt yr^{-1} .

11842

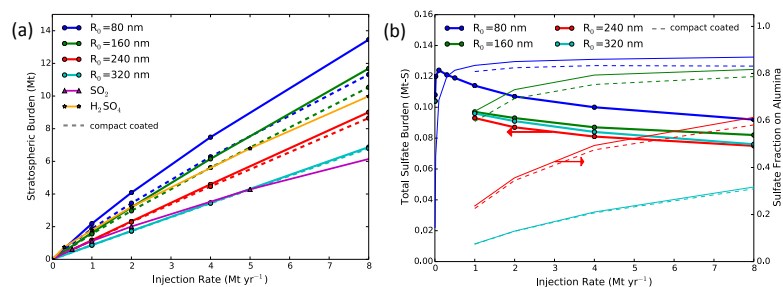


Figure 5. Stratospheric burden of (a) alumina and (b) condensed sulfate vs. injection rate for various sizes of injected alumina monomers. For comparison, we plot sulfate burden in Mt-S as a function of the rate for injection of SO₂ and H₂SO₄ (Pierce et al., 2010) in Mt-S yr⁻¹ along with alumina burden in (a). (b) shows the fate of natural sulfate as a function of alumina injection rate, where the total sulfate burden is plotted on the left-hand axis (thick lines) and the fraction of that burden that is on the alumina particles is shown on the right-hand axis (thin lines). The dashed lines represent simulations in which the coated alumina particles are assumed to become more compact in shape.

11843

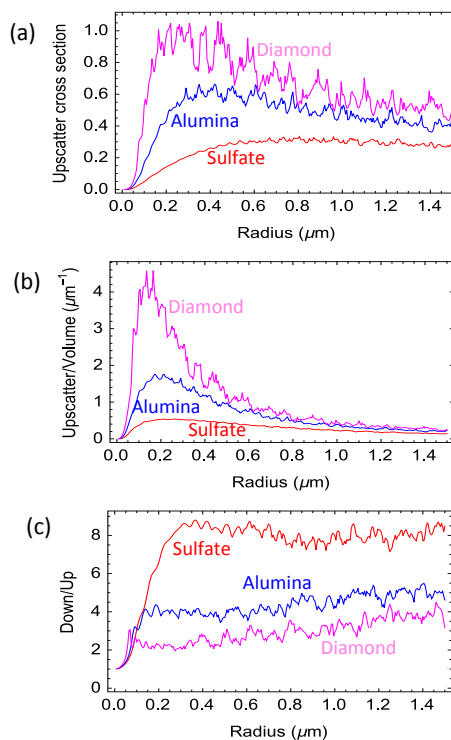


Figure 6. Comparison of radiative scattering properties of alumina and diamond monomers and sulfate aerosol particles as functions of particle radius. (a) shows upscatter cross-sections (dimensionless ratio). (b) shows upscatter cross-section per unit volume (μm⁻¹), and (c) shows the ratio of downscatter cross section to upscatter cross section.

11844

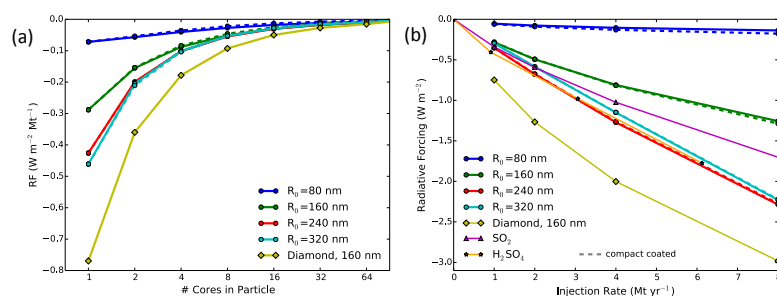


Figure 7. Radiative forcing per megaton burden of globally-averaged alumina or diamond particles as a function of the number of monomer cores per fractal particle (a). Calculated globally-averaged radiative forcing as a function of injection rate for geoengineering scenarios (b). The dashed lines represent simulations in which the coated alumina particles are assumed to become more compact in shape.

11845

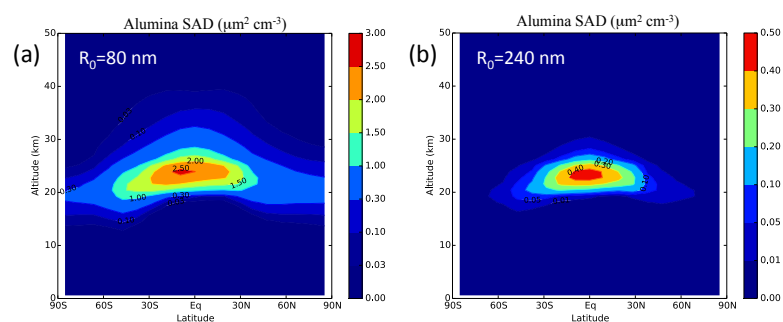


Figure 8. Calculated annual average surface area density ($\mu\text{m}^2 \text{ cm}^{-3}$) of uncoated alumina particles due to geoengineering with 1 Mt yr^{-1} injection of (a) 80 nm alumina monomers and (b) 240 nm alumina monomers.

11846

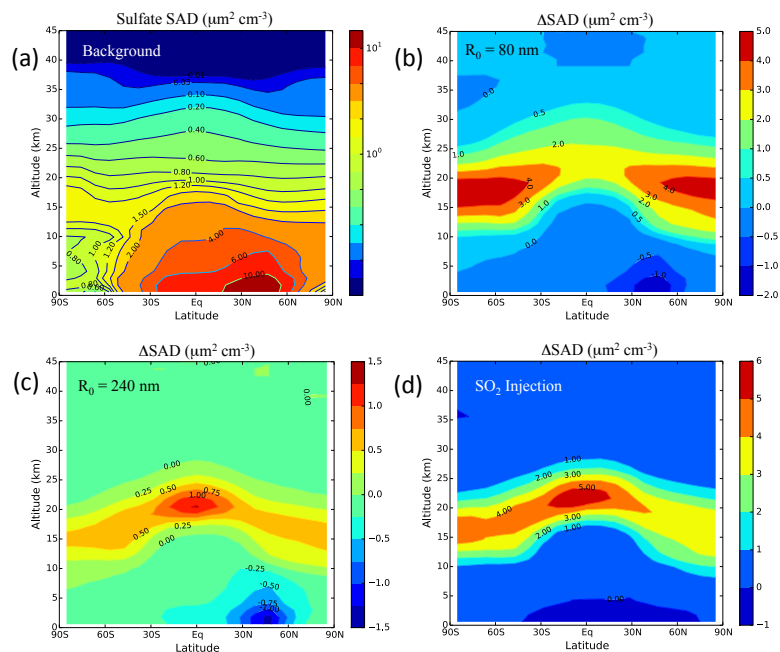


Figure 9. Calculated annual average sulfate surface area density ($\mu\text{m}^2 \text{cm}^{-3}$) of (a) sulfate particles without geoengineering, and surface area density increase ($\mu\text{m}^2 \text{cm}^{-3}$) with geoengineering injections of (b) 1 Mt yr^{-1} of 80 nm alumina monomers and (c) 1 Mt yr^{-1} of 240 nm alumina monomers. (d) shows sulfate aerosol surface area density increase ($\mu\text{m}^2 \text{cm}^{-3}$) with 1 Mt yr^{-1} of SO_2 injection.

11847

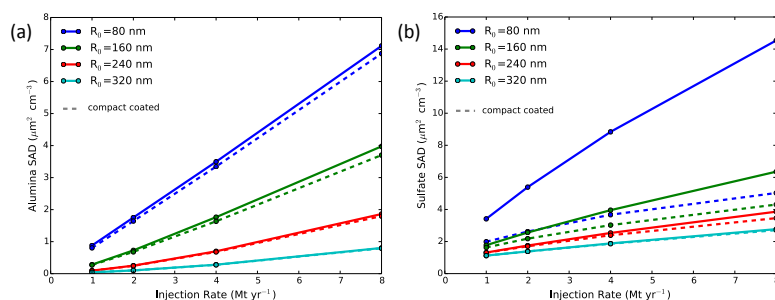


Figure 10. Annual average stratospheric surface area density between 15 and 25 km altitude for (a) uncoated alumina, and (b) total sulfate. The dashed lines represent simulations in which the coated alumina particles are assumed to become more compact in shape.

11848

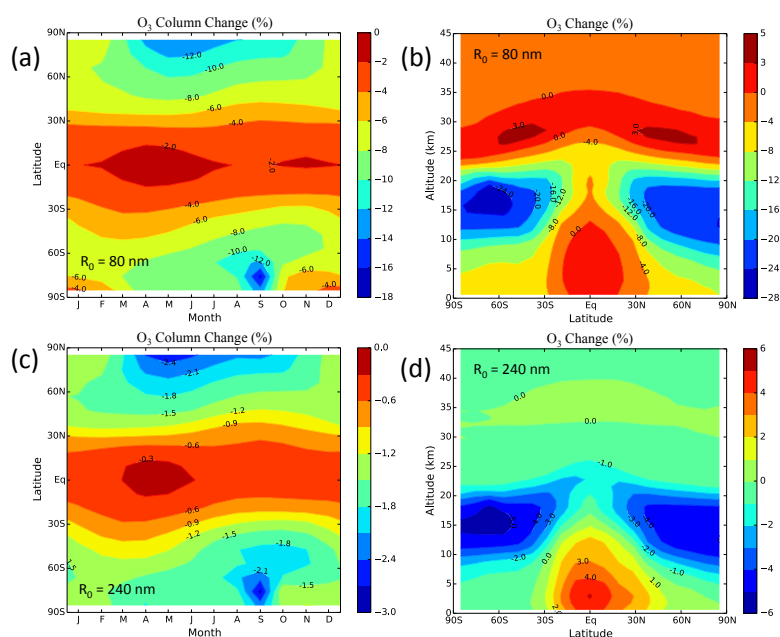


Figure 11. Ozone changes due to injection of alumina aerosol. Column ozone changes (%) are shown as a function of latitude and month (left panels) and annual average local ozone changes (%) as a function of latitude and altitude (right panels). Results are shown for an injection rate of 1 Mtyr^{-1} of 80 nm (top panels) and 240 nm (bottom panels) alumina monomers. Note ozone increases in the upper stratosphere where the NO_x cycle dominates and decreases in the lower stratosphere where the ClO_x and BrO_x cycles dominate.

11849

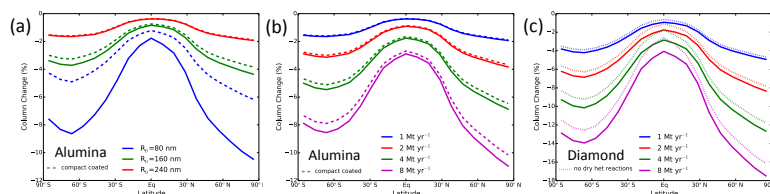


Figure 12. Annual average column ozone change in percent as a function of latitude for (a) cases with 1 Mtyr^{-1} alumina injections as monomers of 80, 160 nm, and 240 nm, (b) cases with injection of 240 nm alumina monomers at rates of 1, 2, 4, and 8 Mtyr^{-1} , and (c) cases with injection of 160 nm diamond monomers at rates of 1, 2, 4, and 8 Mtyr^{-1} . Cases in which coated particles are assumed to become more compact in shape are shown with dashed lines. For diamond, cases without Reaction (R1) occurring on dry diamond particle surfaces are shown with dotted lines.

11850

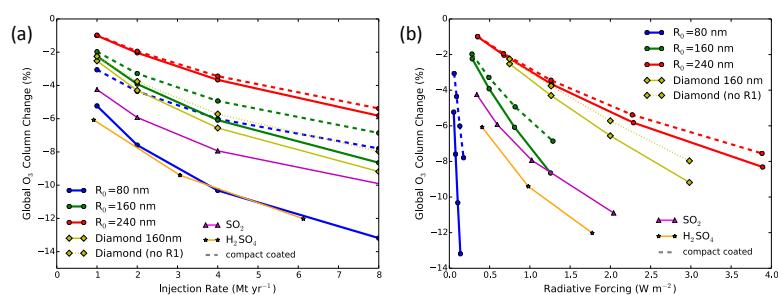


Figure 13. Global average column ozone change (in percent) as **(a)** a function of injection rate and **(b)** as a function of associated radiative forcing. Ozone change for diamond shown with and without Reaction (R1) on uncoated diamond particles. Calculations with SO_2 and H_2SO_4 injections employ the same model to calculate radiative forcing and ozone depletion as for alumina and diamond.